

1 **Combined-cycle gas turbine power plant integration with** 2 **cascaded latent heat thermal storage for fast dynamic responses**

3 Decai Li ^a, Yukun Hu ^b, Dacheng Li ^c, Jihong Wang ^{a,d*}

4 ^a School of Engineering, University of Warwick, Coventry, CV4 7AL, UK

5 ^b School of Management, Cranfield University, Bedford, MK43 0AL, UK

6 ^c Institute of Process Engineering, Chinese Academy of Sciences, Beijing, 100190, P.R. China

7 ^d Huazhong University of Science and Technology, Wuhan, P.R.China

9 **Abstract**

10 The combined-cycle gas turbine (CCGT) power plants are often required to provide the essential fast
11 grid balance service between the load demand and power supply with the increase of the intermittent
12 power generation from renewable energy sources. It is extremely challenging to ensure CCGT power
13 plants operating flexibly and also maintaining its efficiency at the same time. This paper presents the
14 feasibility study of a CCGT power plant combined with the cascaded latent heat storage (CLHS) for
15 plant flexible operation. A 420 MW CCGT power plant and a CLHS dynamic models are developed
16 in Aspen Plus based on a novel modelling approach. The plant start-up processes are studied, and
17 large amount of thermal energy can be accumulated by CLHS during the start-up. For load-following
18 operation, extensive dynamic simulation study is conducted and the simulation results show that the
19 extracted exhaust gas can be used for thermal energy storage charging, and the stored heat can be
20 discharged to produce high temperature and high pressure steam fed to the steam turbine. Besides, the
21 stored heat can also be used to maintain the heat recovery steam generator (HRSG) under warm
22 condition to reduce plant restart-up time. The simulation results demonstrate that the integration of
23 CLHS with CCGT power plant is feasible during the start-up, load-following and standstill
24 operations.

25
26 **Keywords:** combined-cycle gas turbine; cascaded latent heat storage; flexible operation; dynamic
27 modelling; Aspen Plus

29 **Highlights:**

- 30 • Dynamic modelling of combined-cycle gas turbine power plant with thermal storage.
- 31 • Cascaded latent heat storage integration strategies to plant operation processes.
- 32 • Complete system dynamic simulations of the plant with cascaded latent heat storage.
- 33 • Quantified analysis of stored and released thermal energy for different strategies.

35 **1. Introduction**

36 Combined-cycle power generation technology has been developed and served as an effective means
37 for base load supply worldwide since the 1960s due to its inherent advantages in high efficiency and
38 operational flexibility [1]. Although the technology in design and operation of combined-cycle gas

*Corresponding author at: School of Engineering, University of Warwick, UK.
E-mail addresses: jihong.wang@warwick.ac.uk (Prof. J. Wang)

39 turbine (CCGT) plants is now widely available, CCGT plants face new technical challenges nowadays
40 in terms of efficient flexible operation to support the integration of intermittent renewable energy.
41 Over the past 10 years, the capacity of intermittent renewable energy has increased dramatically,
42 which has a significant impact on maintaining the balancing of the power generation and demand.
43 This forces CCGT power plants into a role change: from base load supply to fast response operating
44 services. This has led to a series of potential issues, such as low plant operation energy efficiency, low
45 load factors, and potentially shortened plant life time. To address those issues, this paper investigates
46 a new potential solution – to integrate the plant with thermal storage to create an energy buffer for fast
47 energy dispatch to support plant flexible operation.

48

49 In recent years, the study on flexible plant operation has started being given important consideration
50 and several studies the start-up process of CCGT power plants are reported [2, 3]. Those paper
51 focused on optimizing the start-up process, but the dynamic performance of CCGT power plants
52 operating flexibly under different load conditions have not been extensively studied. With the increase
53 of renewable generation, the impact of passive operation of power plants during load changes has
54 received more attention. The flexible operation of CCGT power plants could enhance the stability of
55 the grid dynamics and maximise short-term high profits, but it will lead to a significant reduction in
56 the lifetime of the power plant equipment [4]. Therefore, many solutions have been proposed to
57 enhance the flexible output of the power plant without compromising its residual life, such as
58 integrated with energy storage systems. CCGT power plants integrated with electrical energy storage
59 was proposed to compensate the intermittent solar power generation [5]. Various thermal power
60 plants integrated with thermal energy storage (TES) were proposed to align power or heat generation
61 with the load demand, including solar thermal power plants [6-8], combined heat and power (CHP)
62 plants [9], and conventional fossil fuel power plants [10, 11]. One study is reported that CCGT power
63 plant integrated with a CO₂ capture unit to achieve load-following operations [12]; oxy-fuel power
64 plant integrated with air separation unit (ASU) to help respond load changes through peak and
65 off-peak operations [13, 14].

66

67 Realisation of dynamic modelling of CCGT power plant processes is still a challenge task. Recently,
68 several studies on dynamic modelling of different types of power plants have been published. Hübel
69 et al. developed a coal-fired power plant model for start-up optimisation [15]. Zhao et al. developed a
70 supercritical coal-fired power plant model using the GSE software to explore strategies of improving
71 operational flexibility [16]. A dynamic model of adiabatic compressed air energy storage plant with
72 packed bed thermal storage was presented in [17]. However, the work on the development of dynamic
73 models for CCGT power plants is very limited, besides a combined-cycle power plant was modelled
74 using software Apros [1] and three different dynamic models of the same CCGT power plant
75 presented in [4].

76

77 In addition, with the maturity of commercial software for process simulations, various process
78 simulators such as Aspen Plus[®] are available and have been widely employed for process simulation
79 purposes by industrial entities since the late 1990s [18-21]. However, all of these studies are based on
80 steady state models. To assess the efficiently flexible plant operation, it is essential to present the
81 dynamic behaviour of variable load demand. Therefore, to derive the CCGT power plant and CLHS
82 dynamic models is the core of the study. This paper will propose a novel modelling approach to

83 address the limitation and capture the main dynamic behaviour of the simulated system in Aspen Plus
84 by incorporated an external dynamic model.

85

86 From the known literature, it is noticed that CCGT power plant integration with cascaded latent heat
87 storage (CLHS) for flexible plant operation has not been reported. The scope of the paper is thus
88 concerned with the flexible operations of the CCGT power plant through integration of CLHS to the
89 plant process. A novel modelling approach is developed and used for study of the integrated dynamic
90 behaviours. This approach incorporates an “explicit difference method” based CLHS models into the
91 “sequential modular strategy” based CCGT power plant model in Aspen Plus, while further taking
92 into account the charging and discharging processes within the different phase change material (PCM)
93 layers. A 420 MW triple-pressure CCGT power plant model is developed to investigate its potential
94 integration strategies with CLHS which stores thermal energy during the start-up processes; to operate
95 flexibly during the load-following operation; and to keep heat recovery steam generator (HRSG)
96 warm during the standstill period.

97

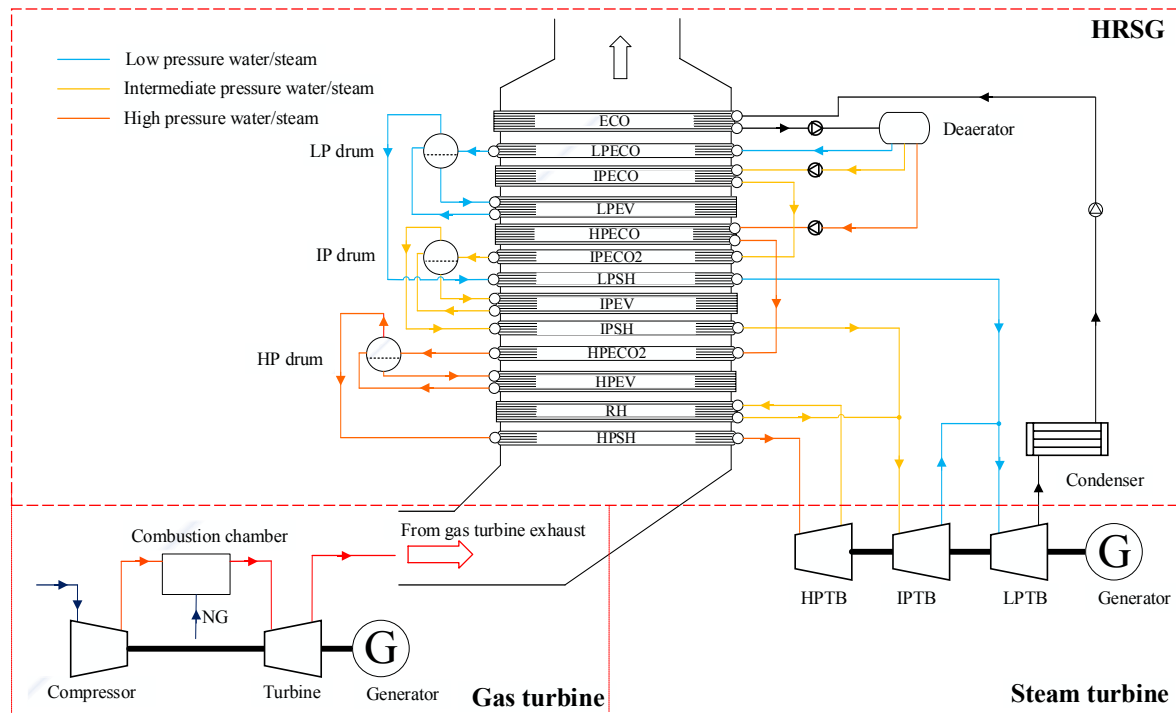
98 This paper is organised as follows: Section 2 brief describes the CCGT power plant and its operating
99 conditions; Section 3 presents the mathematical models of the gas turbine, HRSG, steam turbine, and
100 CLHS; Section 4 offers results and discussion of the proposed integration strategies; finally, in
101 Section 5 conclusions in relation to this overall study are drawn, with clearly outlined suggestions for
102 future exploitation.

103

104 **2. Power plant description**

105 A CCGT power plant generally consists of the gas turbine, HRSG and steam turbines, as shown in
106 Figure 1. Air is compressed via a compressor and is mixed with natural gas (NG) in the combustion
107 chamber for combustion, then hot combustion gas expands in the gas turbine, which forms a Brayton
108 cycle; the heat from the gas turbine exhaust is used to generate steam for steam turbine, that is, the
109 heat passes through the HRSG to heat the water flow, which formulates a Rankine cycle. In this way,
110 the CCGT power plant can achieve a much higher thermal efficiency than a single cycle gas turbine
111 power plant, because the waste heat from the gas turbine exhaust is recovered via the HRSG which is
112 then used by the steam turbines for electricity generation.

113



114

115

Figure 1: The schematic of a 420 MW CCGT power plant.

116

117 A 420 MW CCGT power plant is used for this study and the plant which has three pressure levels
 118 steam drums (HP, IP, and LP) [22], as shown in Figure 1. The CCGT power plant rated state are listed
 119 in Table 1.

120

121 Table 1: Parameters of developed CCGT power plant.

Parameter	Value
Gas turbine power	285 MW
Steam turbine power	135 MW
Exhaust gas mass flow rate	$685 \text{ kg} \cdot \text{s}^{-1}$
Exhaust gas temperature	846 K
Feed water flow rate	$108 \text{ kg} \cdot \text{s}^{-1}$
High pressure steam turbine inlet pressure	140 bar
Intermediate pressure steam turbine inlet pressure	25 bar
Low pressure steam turbine inlet pressure	6 bar
Low pressure steam turbine outlet pressure	0.05 bar

122

123 3. Dynamic modelling of CCGT power plant and thermal energy storage

124 Aspen Plus was used to develop the dynamic model of the CCGT power plant. The PR-BM property
 125 method [23] was chosen for the physical property calculation of the gas cycle, and STEAMNBS
 126 property method [24] was chosen for the physical property calculation of the water-steam cycle
 127 calculation. To implement the dynamic modelling, the built-in 'calculator' block was used to define
 128 time-dependent variables. The sequential model approach is used for simulation of the whole system.
 129 It takes modules as basic computational unit and through sequential calculation of each modules to

130 solve the model. The sequential model approach is widely used for the process modelling, since it
 131 improves the accuracy of the model and reduces the difficulty of system modelling and solving.

132

133 3.1 Gas turbine section modelling

134 The gas turbine section consists of three components: a compressor, a combustion chamber, and a
 135 turbine. For the compressor, it was modelled as a polytropic compression process that gives a more
 136 accurate calculation of the power required for multi-state compressor, and its power consumption can
 137 be calculated by Eq. (1) [22]:

$$138 \quad W_{in,ideal} = \left(\frac{\gamma}{\gamma-1} \right) P_{in} V_{in} \left[\left(\frac{P_{out}}{P_{in}} \right)^{(\gamma-1)/\gamma} - 1 \right], \quad (1)$$

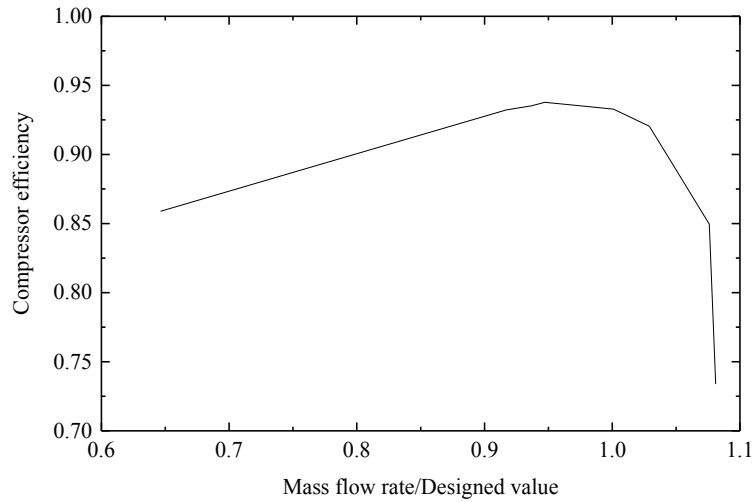
$$139 \quad W_{in} = \frac{W_{in,ideal}}{\eta_c}, \quad (2)$$

140 where, $W_{in,ideal}$ is the power consumption under ideal polytropic condition, γ is the specific heat
 141 ratio, P_{in} is the inlet pressure, V_{in} is the inlet volume, P_{out} is the outlet pressure, W_{in} is the real
 142 power consumption, and η_c is the compressor polytropic efficiency.

143

144 The mechanical efficiency of the compressor used in the simulation is 0.985. The actual polytropic
 145 efficiency of compressor varies with mass flow rate and can be determined by Figure 2 [25]. The
 146 efficiency curve is formulated by using several high-order polynomial equations, in order to minimise
 147 errors. And then the polytropic efficiency is incorporated into Aspen Plus by a FORTRAN subroutine,
 148 and updated each time-step based on the instant compressor mass flow rate.

149



150

151 Figure 2: Compressor efficiency curve.

152

153 The temperature of the compressor outlet stream is given by:

$$154 \quad T_{out} = \frac{T_{in}}{\eta_c} \left[\left(\frac{P_{out}}{P_{in}} \right)^{(\gamma-1)/\gamma} - 1 \right] + T_{in}, \quad (3)$$

155 where, T_{out} is the outlet temperature, and T_{in} is the inlet temperature. The air composition used in
 156 modelling are given in Table 2.

157

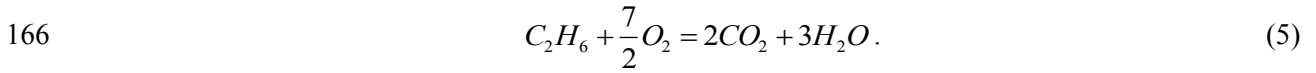
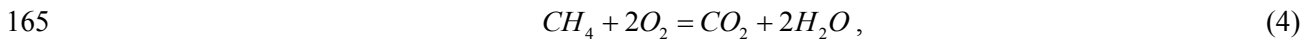
158

159 Table 2: Air composition in molar fraction [26].

Components	Molar Fraction (%)
N_2	75.67
O_2	20.35
H_2O	3.03
CO_2	0.345
Others	0.915

160

161 The natural gas composition used in the modelling is given in Table 3. It consists of methane, ethane,
 162 propane, nitrogen, carbon dioxide, and other gases and the methane and ethane account make up more
 163 than 99% of the total volume [27]. Therefore, only two reactions are considered in the combustion
 164 process:



167

168 Table 3: Nature gas composition in molar fraction.

Components	Molar Fraction (%)
CH_4	98.57
C_2H_6	0.82
N_2	0.6
CO_2	0.01

169

170 For the turbine, it was modelled as an isentropic process, and its output power is calculated by Eq. (6)
 171 [22]:

$$172 \quad W_{out, ideal} = -\left(\frac{\gamma}{\gamma-1}\right) P_{in} V_{in} \left[\left(\frac{P_{out}}{P_{in}}\right)^{(\gamma-1)/\gamma} - 1 \right], \quad (6)$$

$$173 \quad W_{out} = \eta_t W_{out, ideal}, \quad (7)$$

174 where, $W_{out, ideal}$ is the turbine output power under ideal isentropic condition, W_{out} is the real turbine
 175 output power, and η_t is the isentropic efficiency.

176

177 The isentropic efficiency of the turbine is defined as [28]:

$$178 \quad \eta_t = 0.9[1 - 0.3(1 - \dot{n}_t)^2](\dot{n}_t / \dot{m}_t)(2 - \dot{n}_t / \dot{m}_t) \quad (8)$$

179 where, \dot{n}_t is the ratio of rotating speed to its designed value, and \dot{m}_t is the ratio of mass flow rate to
 180 its designed value.

181

182 The temperature of the turbine outlet stream is given by:

$$183 \quad T_{out} = T_{in} - \eta_t T_{in} \left[1 - \left(\frac{P_{out}}{P_{in}}\right)^{(\gamma-1)/\gamma} \right]. \quad (9)$$

184

185 *3.2 HRSG section modelling*

186 The HRSG is modelled as a group of heat exchangers in this study. The exhaust gas from the gas
 187 turbine enters the HRSG, where the waste heat is recovered to produce steam at different pressure
 188 levels (HP, IP, and LP). The heat exchanger dynamic model was developed based on energy and mass
 189 balance equations.

190
 191 The energy conservation equation is given by [29, 30]:

$$192 \quad V\rho \frac{\partial h}{\partial t} + m \frac{\partial h}{\partial z} dz = Q + W, \quad (10)$$

193 and mass balance gives [3]:

$$194 \quad \frac{\partial \rho}{\partial t} + \frac{\partial \rho v}{\partial z} = 0 \quad (11)$$

195
 196 The heat flux can be calculated by Eq. (12):

$$197 \quad Q = UA\Delta T. \quad (12)$$

198
 199 In order to capture the dynamics of the heat exchanger, the heat exchanger is discretized into several
 200 zones, as shown in Figure 3, each of which obey both energy and mass conservation equations [29].
 201

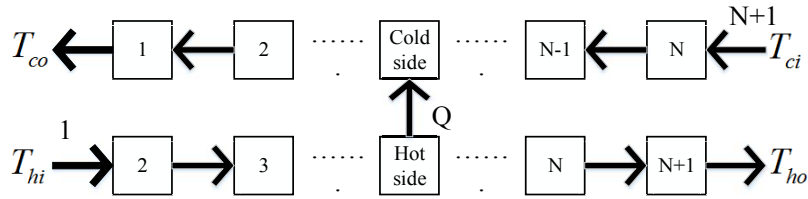


Figure 3: Cell model of the counter current heat exchanger.

202
 203
 204
 205 The instantaneous temperature change of cold stream can be calculated by Eq. (13):

$$206 \quad \frac{dT_{c,i}}{dt} = \frac{UA_i(T_{h,i+1} - T_{c,i}) - m_c c_{p,ci}(T_{c,i} - T_{c,i+1})}{V_i \rho_{c,i} c_{p,ci}}. \quad (13)$$

207
 208 Similarly, the instantaneous temperature change of hot stream can be calculated by Eq. (14):

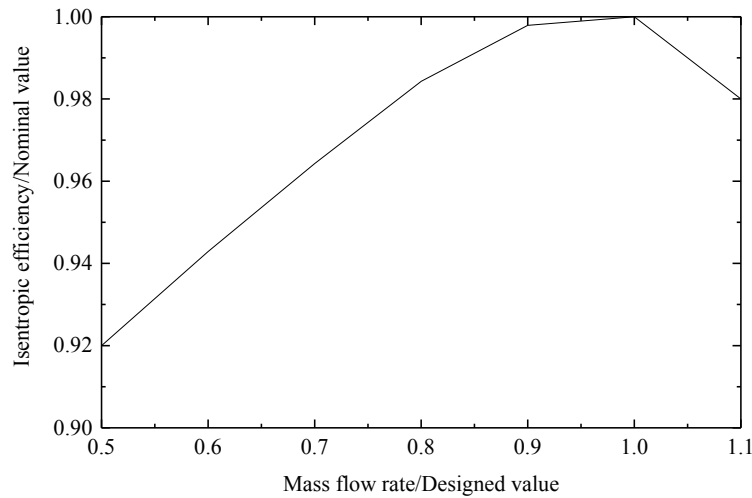
$$209 \quad \frac{dT_{h,i}}{dt} = \frac{-UA_i(T_{h,i} - T_{c,i-1}) + m_h c_{p,hi}(T_{h,i-1} - T_{h,i})}{V_i \rho_{h,i} c_{p,hi}}. \quad (14)$$

210
 211 In the model simulation, the thermodynamic properties (e.g. heat capacity and density) of the exhaust
 212 gas and water/steam are updated at every time-step based on the current temperature and pressure
 213 using Aspen Plus's thermodynamic database.

214
 215 *3.3 Steam turbine section modelling*

216 Three levels of steam generated by the HRSG are used to spin the corresponding three steam turbines:
 217 high pressure turbine (HPTB), intermediate pressure turbine (IPTB), and low pressure turbine (LPTB).
 218 The development of the steam turbine models uses the same thermodynamic principles as the gas
 219 turbine model development, which is presented in Section 3.1. The actual isentropic efficiency of

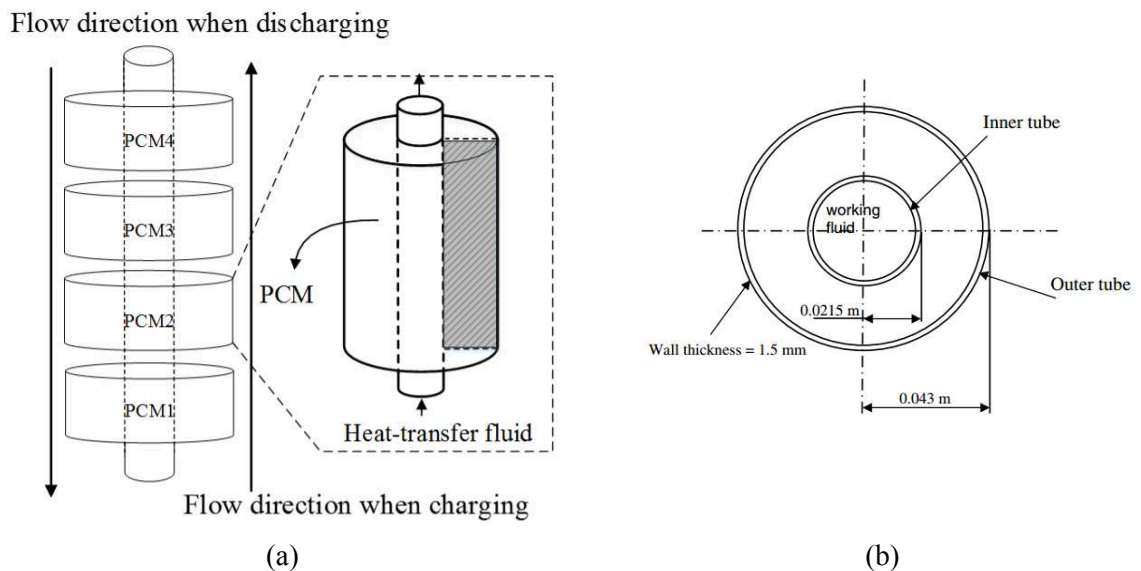
220 steam turbine varies with mass flow rate and can be determined by Figure 4 [31]. The nominal values
 221 of HPTB, IPTB, and LPTB used in the simulation were 0.88, 0.88 and 0.85, respectively.



222
 223 Figure 4: Steam turbine isentropic efficiency curve.
 224

225 **3.4 Cascaded latent heat storage (CLHS)**

226 In the CLHS system, thermal energy is transferred to the storage media during charging, and is
 227 released in later discharging step. There are mainly three types of thermal energy storage: sensible
 228 heat storage, latent heat storage, and chemical heat storage [7]. The latent heat storage will be used for
 229 this study because its energy density is much higher than sensible heat storage [32, 33] and the cost is
 230 lower than chemical heat storage. Besides, heat transfer irreversibility of a latent heat storage system
 231 can be significantly reduced using cascaded phase change materials [7].
 232



233 Figure 5: Structure of a signal CLHS set (a) and its sectional view (b) [34].
 234

235 The designed CLHS system in this study consists of four PCM layers, which are NaCl&CaCl₂
 236 (PCM1), MgCl₂&NaCl&KCl (PCM2), LiCl&LiOH (PCM3), LiNO₃&NaNO₃&KCl (PCM4). These
 237 PCM layers are arranged in the direction of charging flow as shown in Figure 5 (a) and their
 238 thermodynamic properties are listed in Table 4. The basic structure of the CLHS system consists of

239 two vertical concentric tubes filled with four cascaded PCM layers in between [34], as shown in
 240 Figure 5 (a), with a radius of 0.0215 m for the inner tube and 0.043 m for the outer tube, a wall
 241 thickness of 0.0015 m, and a height of 20 m (5 m for each PCM layer), as shown in Figure 5 (b). The
 242 entire CLHS system consists of 5600 sets of such concentric tubes in parallel.

243

244 The consideration for such an arrangement is that heat is required to be quickly absorbed or released
 245 during the charging or discharging processes. The temperature difference decreases in the flow
 246 direction of the working fluid in a single PCM layer and results in a decrease in the heat transfer rate
 247 and thereby mediocre performance. The multiple PCM layers with different phase change temperature
 248 are cascaded in decreasing order of phase change temperature, so despite the decrease in the heat
 249 transfer fluid temperature the temperature difference can still be maintained constantly during
 250 charging [35]. For the discharging, the heat-transfer fluid flows in the opposite direction so that the
 251 PCM layers are arranged in ascending order of phase change temperature, thus maintaining the
 252 temperature difference between the PCM layers and the heat-transfer fluid.

253

254 At rated state, the temperature of gas turbine exhaust gas is 846 K, therefore the material PCM1 is
 255 chose whose melting temperature is 773 K. In this way, the outlet temperature of PCM1 will not
 256 exceed 773 K for the charging process. This guarantees the maximum temperature of PCM2 will be
 257 less than 773 K. Moreover, the PCMs have to operate around the melting point to ensure safety and
 258 without poisonous gas generated. For these reasons, the materials listed in Table 4 are selected for the
 259 proposed model.

260

261 Table 4: Thermophysical properties of PCMs [36].

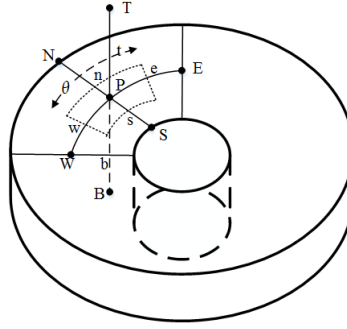
Material	Composition, wt%	Melting temp., K	Latent heat, J/g	Specific heat, J/(g·K)	Density, g/cm ³	Conductivity, W/mK
PCM1	33 (NaCl) 67 (CaCl ₂)	773	280	1	2.16	1.02
PCM2	63 (MgCl ₂) 22.3 (NaCl) 14 (KCl)	658	461	0.96	2.25	0.95
PCM3	37 (LiCl) 63 (LiOH)	535	485	2.4	1.55	1.1
PCM4	55.4 (LiNO ₃) 4.5 (NaNO ₃) 40.1 (KCl)	433	266	1.4	2.21	1

262

263

264 In the CLHS system, the heat transfer process is coupled with heat convection and heat conduction.
 265 Heat transfer fluid transfers heat to the inner tube by means of heat convection. For the heat transfer
 266 from the inner tube to the PCM and the heat diffusion in the PCM, the heat transfer is by means of
 267 heat conduction. The heat loss through the outer tube of the CLHS system is assumed negligible.
 268 Figure 6 shows a portion of a three-dimensional heat conduction grid.

269



270

Figure 6: Three-dimensional heat conduction.

271

272

273 In a cylindrical-coordinate system, the three-dimensional heat conduction equation for the point P in
 274 the Figure 6 is given by [37]:

$$275 \quad \rho c_p \frac{\partial T_P}{\partial t} = \frac{1}{r} \frac{\partial}{\partial r} (rk \frac{\partial T}{\partial r}) + \frac{1}{r} \frac{\partial}{\partial \theta} (k \frac{\partial T}{\partial \theta}) + \frac{\partial}{\partial z} (k \frac{\partial T}{\partial z}), \quad (15)$$

276 where, subscript P denotes the point P shown in Figure 6.

277

278 Due to the cylinder is symmetrical, the unique temperature in θ direction is assumed. Therefore, the
 279 heat conduction equation in the cylinder is given by [38]:

$$280 \quad \rho c_p \frac{\partial T_P}{\partial t} = \frac{1}{r} \frac{\partial}{\partial r} (rk \frac{\partial T}{\partial r}) + \frac{\partial}{\partial z} (k \frac{\partial T}{\partial z}). \quad (16)$$

281

282 The discretization equation is obtained by integrating the differential equations in the control volume
 283 over the time interval from t to $t + \Delta t$. The discretized equation is shown as follows [37]:

$$284 \quad a_p T_P = a_N [f T_N - (1-f) T_N^0] + a_S [f T_S - (1-f) T_S^0] + a_T [f T_T - (1-f) T_T^0] + \quad (17)$$

$$a_B [f T_B - (1-f) T_B^0] + [a_p^0 - (1-f) a_N - (1-f) a_S - (1-f) a_T - (1-f) a_B] T_P^0,$$

$$285 \quad \text{where, } a_N = \frac{kr_n \Delta \theta \Delta z}{(\delta r)_n}, \quad a_S = \frac{kr_s \Delta \theta \Delta z}{(\delta r)_s}, \quad a_T = \frac{k0.5(r_n + r_s) \Delta \theta \Delta r}{(\delta z)_t}, \quad a_B = \frac{k0.5(r_n + r_s) \Delta \theta \Delta r}{(\delta z)_b},$$

286 $a_p^0 = \frac{\rho c \Delta V}{\Delta t}$, and $a_p = fa_N + fa_S + fa_T + fa_B + a_p^0$. Subscripts N and n are north side points, S and s
 287 are south side points, T and t are top side points, and B and b are bottom side points, as shown in
 288 Figure 6.

289

290 The ΔV is the volume of the control volume, which is given by:

$$291 \quad \Delta V = 0.5(r_n + r_s) \Delta \theta \Delta r \Delta z. \quad (18)$$

292

293 There are three methods available for solving the discretised partial differential equation that depends
 294 on the value of the weighting factor (f). In particular, $f = 0$ leads to the explicit scheme, $f = 0.5$
 295 to the Crank-Nicolson scheme, and $f = 1$ to the fully implicit scheme. The explicit scheme is used to
 296 discretize the differential equation in this study, as follows:

$$297 \quad a_p T_P = a_N T_N^0 + a_S T_S^0 + a_T T_T^0 + a_B T_B^0 + (a_p^0 - a_N - a_S - a_T - a_B) T_P^0. \quad (19)$$

298

299 This means that T_p is not related to other unknown temperatures such as T_N , T_S , T_T and T_B , but it is
 300 explicitly related to the known temperatures T_N^0 , T_S^0 , T_T^0 and T_B^0 . The main advantage of the
 301 explicit scheme is that it can solve partial differential equations non-iteratively by direct calculation.
 302 However, for the explicit scheme, the time step (Δt) has to be small enough to ensure the simulation
 303 result accuracy and the time step in this study is set to 0.001s.

304

305 However, during the phase change, the temperature of the PCM is maintained at the melting
 306 temperature [39]. Therefore, the above equations are only used for calculations under pure solid and
 307 liquid conditions. To over the melting process, the following equation is introduced to calculate the
 308 enthalpy change during PCM melting [7, 32, 38]:

$$309 \quad \rho \frac{\partial H_p}{\partial t} = \frac{1}{r} \frac{\partial}{\partial r} (rk \frac{\partial T}{\partial r}) + \frac{\partial}{\partial z} (k \frac{\partial T}{\partial z}). \quad (20)$$

310

311 The discretization equation is given by:

$$312 \quad a_p' (H_p - H_p^0) = a_N T_N^0 + a_S T_S^0 + a_T T_T^0 + a_B T_B^0 + (-a_N - a_S - a_T - a_B) T_p^0, \quad (21)$$

313 where, $a_p' = \frac{\rho \Delta V}{\Delta t}$. The H_p^0 is the known enthalpy (old enthalpy), and the discretization method is
 314 also explicit scheme. Due to the outer tube is assumed adiabatic, there is no heat conduction on the
 315 boundary. Thus a_T is set as 0 for the topmost side of PCM, a_B is set as 0 for the bottommost side
 316 of PCM, and a_N is set as 0 for the outermost side of PCM.

317

318 The CLHS model is developed based on the above discretized equations and incorporated into Aspen
 319 Plus model through an external FORTRAN subroutine. The thermodynamic properties of the working
 320 fluid are calculated by the Aspen Plus's thermodynamic database, while the properties of the PCMs
 321 are using the data from literature which is listed in Table 4. The validation of the CCGT power plant
 322 and latent heat storage model is presented in the previous publication [31].

323

324 4. Results and discussion

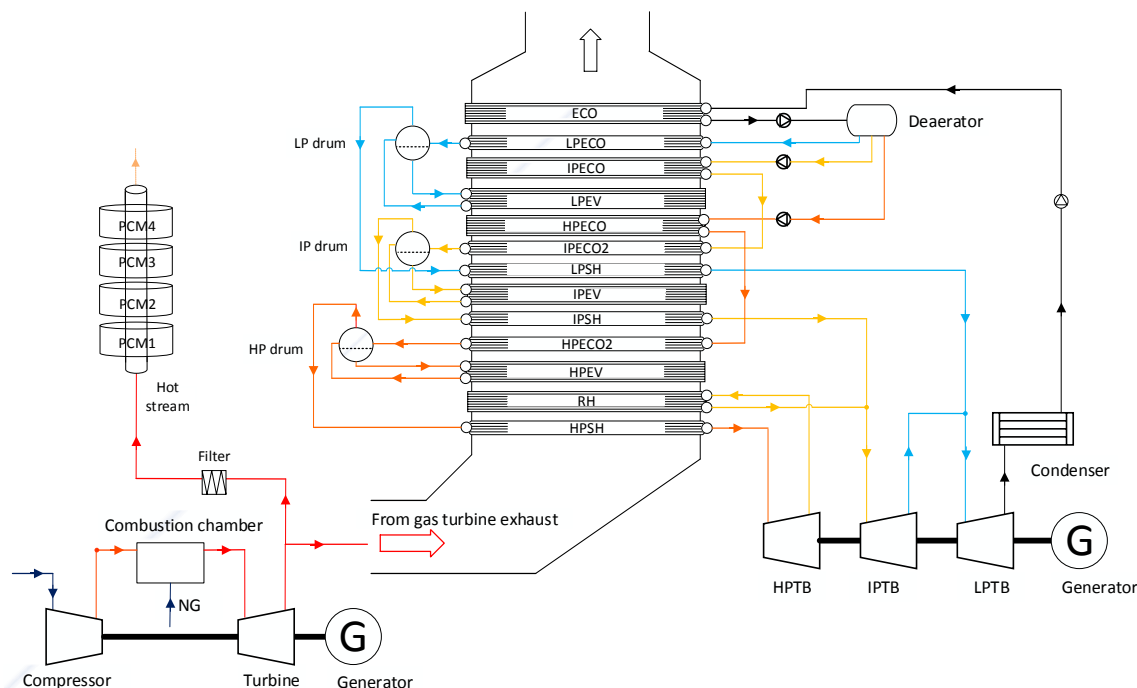
325 This section presents the integration strategies of CCGT power plant with CLHS during the start-up,
 326 load-following operation, and standby, respectively. In particular, the start-up procedure is studied,
 327 and the idea of energy storage during plant start-up is proposed. The paper examines how the
 328 integration of CLHS impact on the performance of the plant regarding to the output power and CLHS
 329 charging or discharging processes. The plant output power can be regulated through variation of
 330 CLHS charging and discharging processes. The stored thermal energy can also be used to keep HRSG
 331 warm during plant standby so as to restart faster.

332

333 4.1 CLHS integration strategy during the plant start-up

334 In practice, although the gas turbine can start-up from cold state to nominal load condition within 20
 335 minutes, it takes up to 170 minutes for the HRSG to reach its nominal load, depending on the initial
 336 temperature state of start-up, that is, hot, warm or cold [40]. This is due to the high thermal stress of
 337 the HRSG section, which is caused by the temperature gradient in metal. In order to reduce thermal
 338 stress of the HRSG, a bypass damper is used to control the gas flow to the HRSG [41]. Therefore,
 339 only a small part of the exhaust gas passes through the HRSG at the start-up, and most of the exhaust
 340 gas is directly discharged into the atmosphere, resulting in energy loss. As described in [42],
 341 approximately 75% of the exhaust gas (513 kg/s in this study) from the gas turbine is discharged into

342 the atmosphere for 25 minutes during the plant start-up. However, this waste energy is potential to be
 343 captured by the CLHS, as shown in Figure 7. The 75% of exhaust gas may first pass through the
 344 CLHS before discharging into atmosphere, and the other 25% of exhaust gas flows into HRSG, during
 345 the plant start-up process. A filter is needed to remove the corrosive gases of the exhaust gas, as
 346 shown in Figure 7, and the gas pressure of CLHS outlet is assumed to be the same as the atmosphere.
 347 In this way, waste heat in the exhaust gas can be captured by the PCM layers in the CLHS.



348
 349 Figure 7: CLHS integration strategy for charging during plant start-up.

350 For PCM layers filled at the same height in the CLHS system, it can be assumed that they have the
 351 same temperature distribution due to their parallel structure [33]. Then the study of the entire CLHS
 352 system can be simplified as a study of one set of concentric tubes (Figure 5 (a)). In order to establish a
 353 reasonable initial temperature distribution of the PCM layers such that a phase change process occurs
 354 in the simulation, a temperature below the phase change point of each PCM is used to start up the
 355 CLHS, as listed in Table 5; when the local temperature reaches the phase transition point, the
 356 temperature distribution of each PCM at that time is its initial temperature distribution, as shown in
 357 Figure 8. The figure presents the temperature distribution of the shaded area in the Figure 5 (a). For
 358 each PCM layer, the phase change temperature is reached first in the lower left corner as expected.
 359 The axial temperature distribution coincides with the exhaust gas in the inner tube, while the radial
 360 temperature distribution also follows the heat conduction from the inside to the outside of the PCM.

361
 362 Table 5: Parameter setting used to establish initial temperature distribution.

Layer	Start-up temp., K	Phase change temp., K	Initial temperature distribution
PCM4	387.7	433	Figure 8 (a)
PCM3	502	535	Figure 8 (b)
PCM2	596	686	Figure 8 (c)
PCM1	697	773	Figure 8 (d)

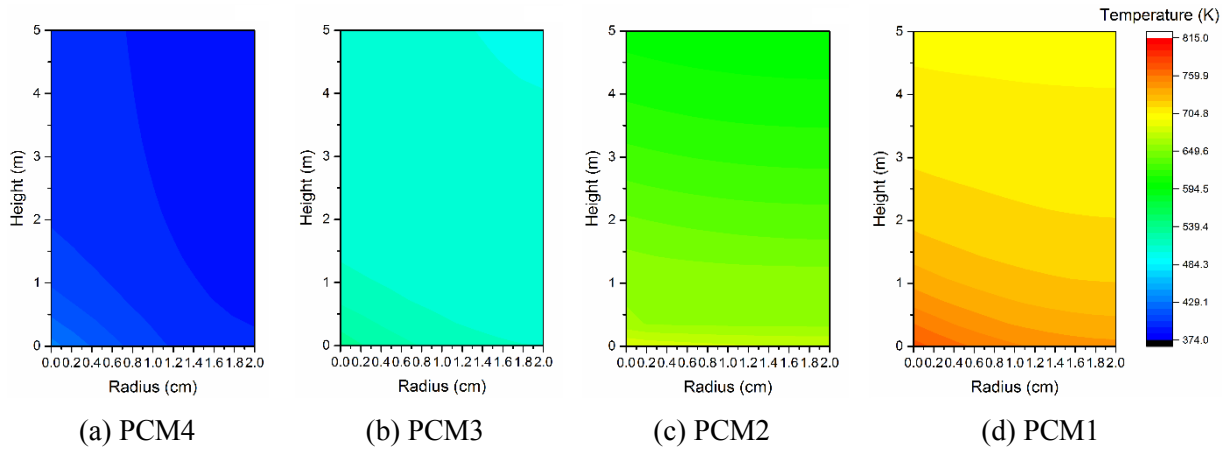


Figure 8: Initial temperatures distribution of different PCM layers.

After 1500 seconds of simulated charging process, waste heat in the exhaust gas is further diffused and stored in the PCMs. The lowest local temperature of each PCM layer reaches the phase transition point, and the temperature in the region where the local temperature is higher than the phase change point continues to increase after undergoing the phase change process. The updated temperature distribution of different PCM layers are shown in Figure 9. The plotted temperature is the right side of the concentric tubes (see Figure 5 (a)) and the gas flows from bottom to top, therefore, the heat diffuses from left side to right side, and from bottom side to top side as well.

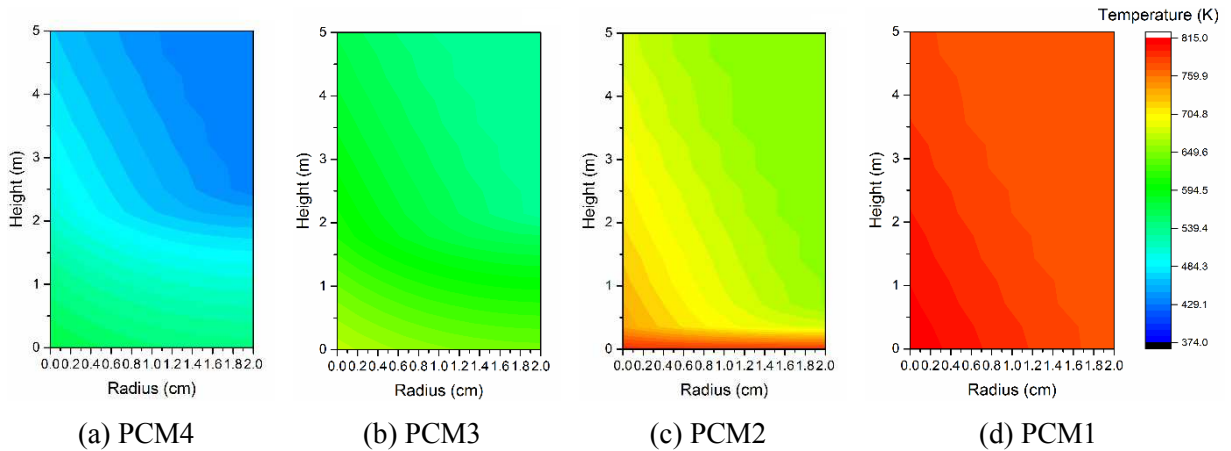


Figure 9: Temperature distribution of different PCM layers at the end of charging in the start-up operation.

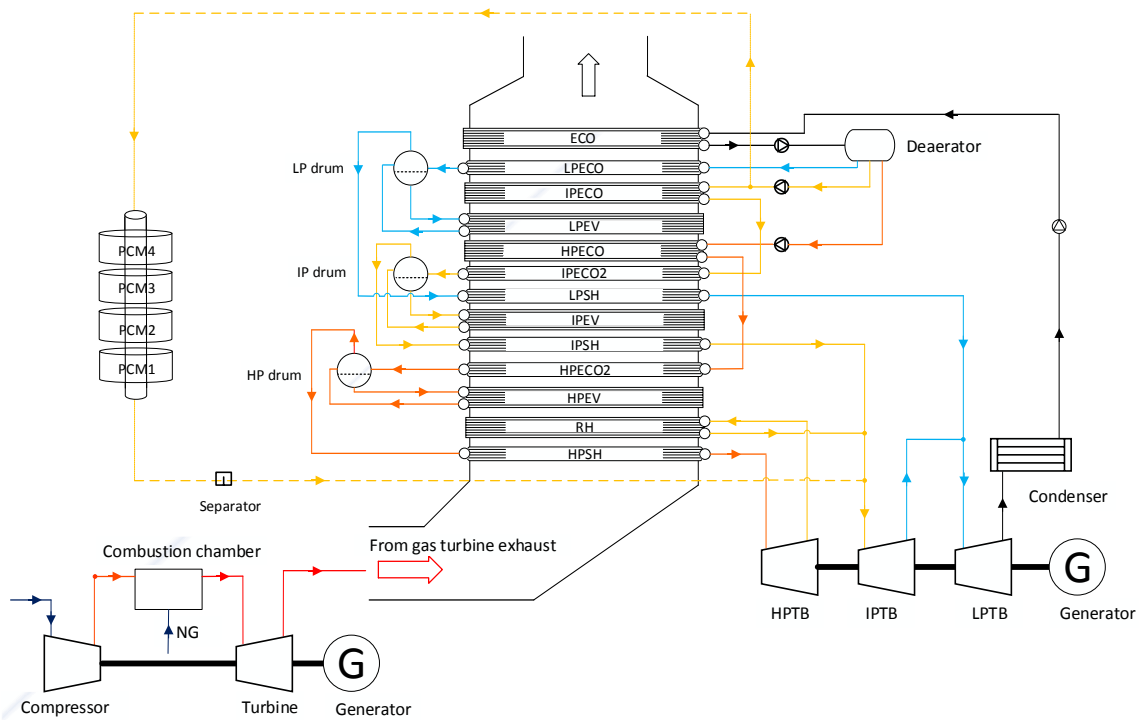
The stored thermal energy ($Q_{storage}$) can be calculated by [7]:

$$Q_{storage} = M_{PCM}[\Delta T \cdot c_p + L], \quad (22)$$

where, M_{PCM} is the mass of PCM, ΔT is the temperature change, c_p is the heat capacity, and L is the latent heat. According to the calculation, a total of 327 GJ heat is stored in the CLHS system in the 1500 seconds, and from left to right each PCM layer stores heat of 88 GJ, 101 GJ, 83 GJ, and 55 GJ, respectively.

382 *4.2 CLHS integration strategy during load-following operation*

383 In addition to avoiding the energy loss of the exhaust gas during the start-up process, the real-time
 384 output power of the CCGT power plant can be regulated within a certain range by the CLHS charging
 385 and discharging processes. The response speed of CCGT power plant is mainly limited by the
 386 water-steam cycle, therefore, this section focuses on the utilization strategies of thermal storage in
 387 water-steam cycle. During off-peak time, part of the high-temperature exhaust gas is extracted from
 388 the gas turbine as a heat source for CLHS charging (same as the layout shown in Figure 7). As the
 389 result, the power generated by the steam turbines will be reduced, but the gas turbine section is still
 390 operating under the rated load condition. The minimum steam turbine power is 66 MW when 363 kg/s
 391 exhaust gas by pass to the CLHS for thermal storage. On the contrary, during peak time, part of the
 392 feed water from the deaerator flows into the CLHS, undergoing the reverse process of charging, it
 393 evaporates into high temperature steam, and then leaves CLHS as superheated steam, as shown in
 394 Figure 10. The maximum steam turbine output power increases to 143 MW. In order to produce dry
 395 steam for steam turbine, a separator is needed to separate water droplets from steam. Finally, the
 396 stored thermal energy is released from the CLHS to the feed water, thereby increasing the power
 397 output of the steam turbines.
 398

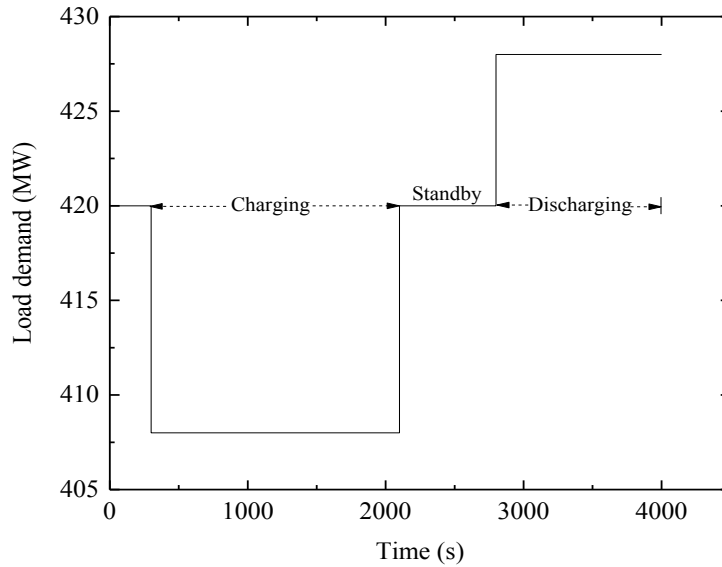


399

400 Figure 10: CLHS integration strategy for discharging during load-following operation.

401 The simulated discharging process is as follows. At beginning, the power plant operates at the
 402 nominal load condition, and the total output power is 420 MW, in which 285 MW is from the gas
 403 turbine and 135 MW is from the steam turbines. Figure 11 shows the designed load demand dynamics.
 404 At the 300th second, the load demand was reduced from 420 MW to 408 MW. After 1800 seconds,
 405 the load demand returned to 420 MW. At the 2800th second, the load demand increased again from
 406 420 MW to 428 MW and lasted 1200 seconds. During this period, the gas turbine has been operating

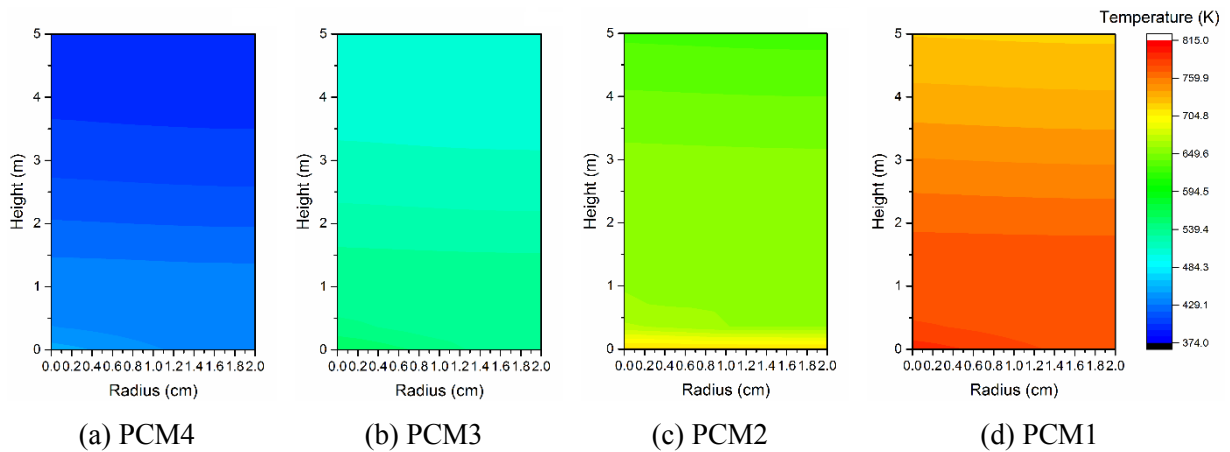
407 under rated conditions with an output power of 285 MW. As a result, the real-time power output of
 408 the power plant is determined by the steam turbines. It should be pointed out that the initial
 409 temperature distribution of the CLHS layers used for the load-following operation simulation is the
 410 same as the initial temperature distribution (Figure 8) in the start-up operation simulation.
 411



412
 413 Figure 11: The desired load demand dynamics during load-following operation.
 414

415 *4.2.1 CLHS charging process*

416 To meeting the load demand reduction from 420 MW to 408 MW, correspondingly the steam turbine
 417 output power was reduced from 135 MW to 123 MW, 60 kg/s of exhaust gas was extracted from the
 418 gas turbine outlet and sent to the CLHS. This is under charging conditions, so the extracted gas also
 419 flows from the bottom of the CLHS to its top, which is the direction along the PCM melting point in
 420 decreasing order. Figure 12 shows the temperature distribution of different PCM layers at the end of
 421 charging in the load-following operation (time = 2160s). Compared to the temperature distribution of
 422 different PCM layers in the start-up operation (Figure 9), the radial temperature difference of each
 423 PCM layer is significantly reduced. This is because the charging time in the load-following operation
 424 is longer than that in the start-up operation. Thus, the thermal diffusion in the PCM is more fully.
 425

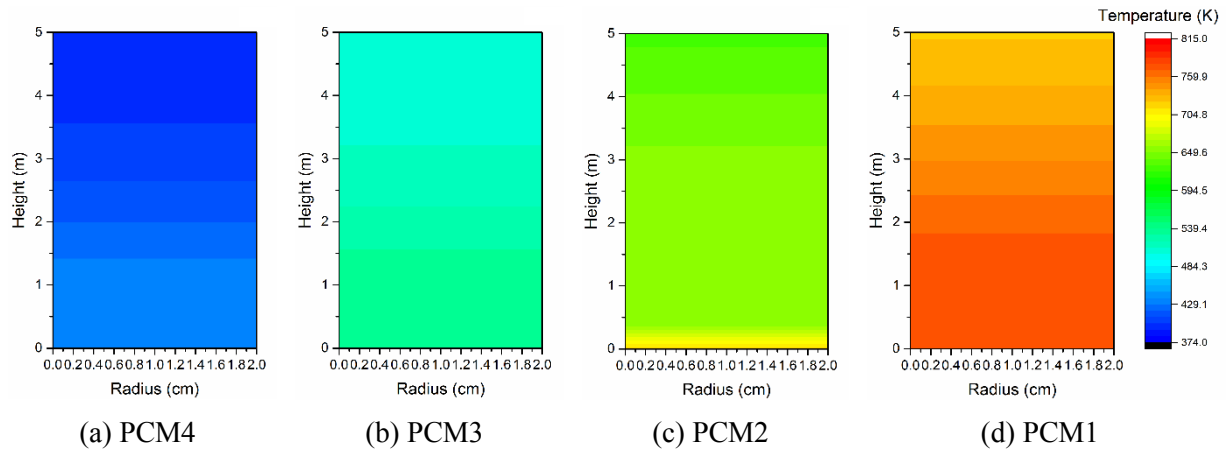


426 Figure 12: Temperature distribution of different PCM layers at the end of charging in the
 427 load-following operation.

428
 429 *4.2.2 CLHS standby process*

430 After charging, the power demand returned to 420 MW, correspondingly the steam turbine output
 431 power returned to 135 MW. Followed by a nominal power demand of 700 seconds, the CLHS was on
 432 standby, i.e. neither charging nor discharging during this period. Figure 13 shows the temperature
 433 distribution of different PCM layers at the end of standby in the load-following operation (time =
 434 2800s). Although there is no heat exchange with external, the heat conduction still occurs inside the
 435 CLHS, thus resulting in a further reduction of the temperature difference in each PCM layer.

436

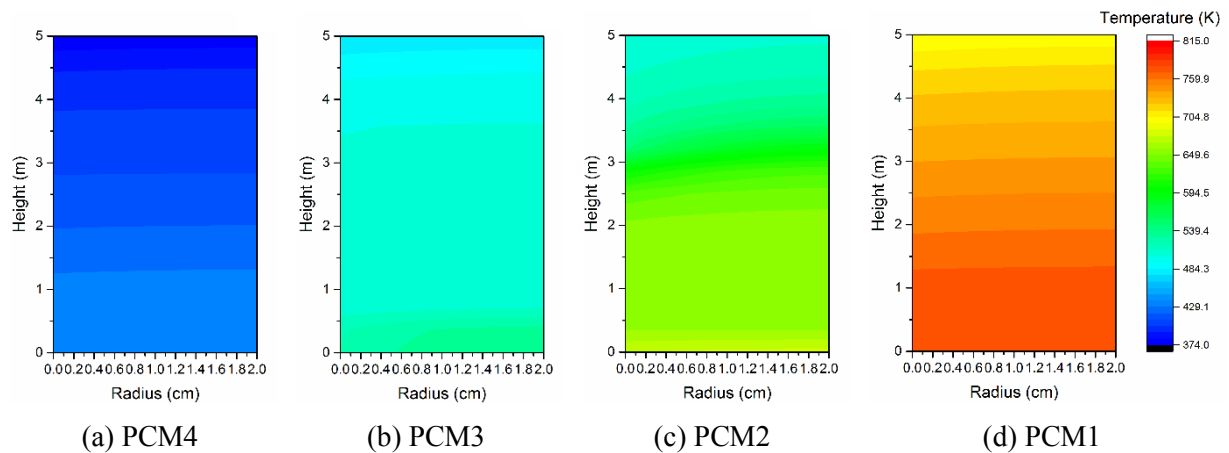


437 Figure 13: Temperature distribution of different PCM layers at the end of standby in the
 438 load-following operation.

439
 440 *4.2.3 CLHS discharging process*

441 To meet the load demand increase from 420 MW to 428 MW, correspondingly the steam turbine
 442 output power was increased from 135 MW to 143 MW, 10 kg/s of superheated steam produced by
 443 CLHS was sent to IPTB. This is under discharging conditions, so the extracted feed water flows from
 444 the top of the CLHS to its bottom, which is the direction along the PCM melting point in ascending
 445 order. Figure 14 shows the temperature distribution of different PCM layers at the end of discharging
 446 in the load-following operation (time = 4000s). Compared to the temperature distribution of different
 447 PCM layers at the end of charging in the load-following operation (Figure 12), the radial temperature
 448 is slowly reduced from the right end to the left end at the same height of each PCM layer. This proves
 449 that an amount of heat has been transferred from the PCM layers to the feed water.

450
 451



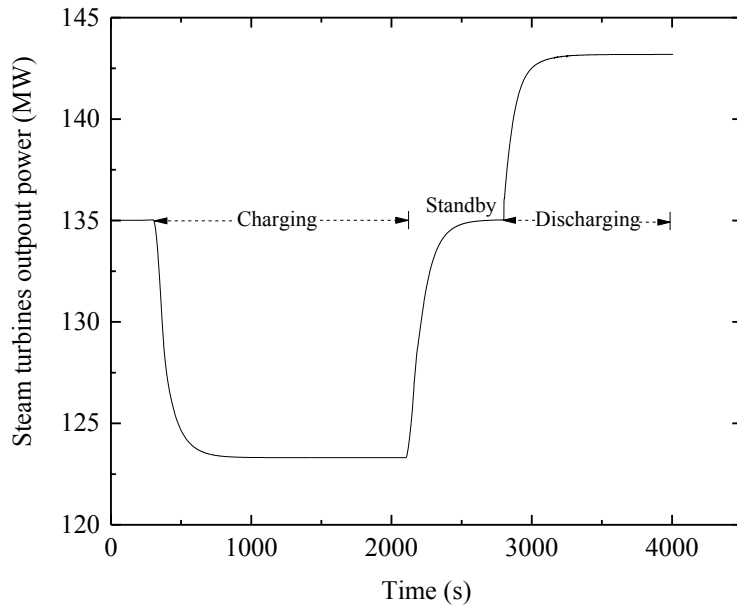
452 Figure 14: Temperature distribution of different PCM layers at the end of discharging in the
 453 load-following operation.

454 It can be seen from the simulation results that since the latent heat energy density is much higher than
 455 the sensible heat, although the temperature change is small, the amount of stored or released is large.
 456 The CLHS system with different melting temperatures can make the temperature difference between
 457 the working fluid and PCM large enough to ensure all PCMs phase changes. So that the CLHS system
 458 makes heat transfer more efficient for both charging and discharging processes.

459
 460 *4.2.4 Load-following dynamics*

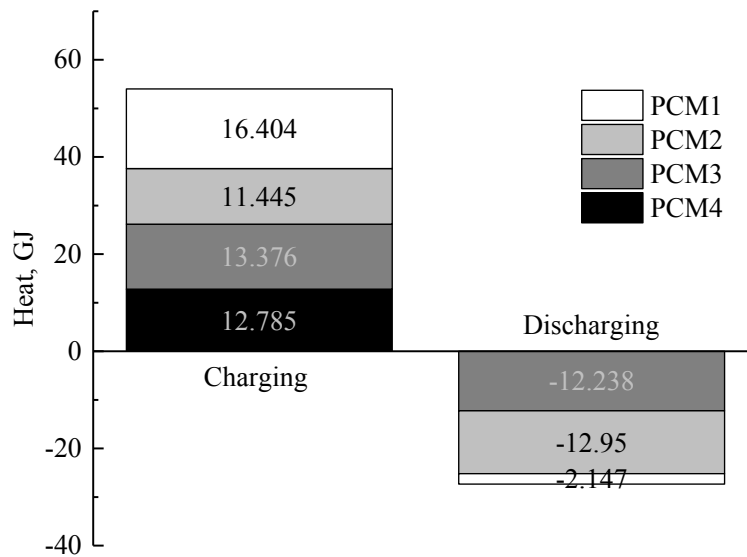
461 Figure 15 shows the real-time output power of the steam turbines during load-following operation.
 462 The steam turbines can correctly respond the load dynamics. Whenever the load changes, the steam
 463 turbines can respond to them within 6 mins. The response time meets the Secondary Frequency
 464 Response requirements of generating units specified in the GB Grid Code [43]. Figure 16 further
 465 reveals the amount of heat stored and released over charging and discharging during load-following
 466 operation. According to the calculation, a total of 54 GJ heat is stored in the CLHS system in the 1860
 467 seconds and a total of 27.5 GJ heat is released to the feed water in the 1200 seconds. It can be seen
 468 that each PCM layer stores a relatively equal amount of heat during charging, but that are very
 469 different during discharging. The discharged heat from PCM4 is very small (0.1714 GJ), therefore it
 470 is not visible from the figure. This is because heat transfer is mainly determined by the heat sink
 471 (PCMs for charging and water for discharging) in both processes. During charging the local initial
 472 temperature of each PCM layer is close to its own phase change temperature and phase change occurs
 473 gradually throughout the PCM layers, so heat is stored primarily through latent heat of phase change
 474 and the thermodynamic reversibility of the process is relatively greater. However, during discharging
 475 the evaporation temperature of water does not change much, which causes its phase change to occur
 476 in only a few layers and the thermodynamic reversibility of the process is relatively smaller. This
 477 explanation can also be verified by the results shown in Figure 17. As can be seen, during charging
 478 the temperature of the exhaust gas entering and exiting each PCM layer crosses its phase change
 479 temperature (Figure 17 (a)), but during discharging only the temperature of the water entering and
 480 exiting the PCM layer 2 and 3 crosses its phase change temperature (Figure 17 (b)). Therefore, based
 481 on the different thermal properties of PCMs and water, it can be expected that there is an optimal
 482 thickness for each phase change layer to maximize the charge and discharge performance.

483



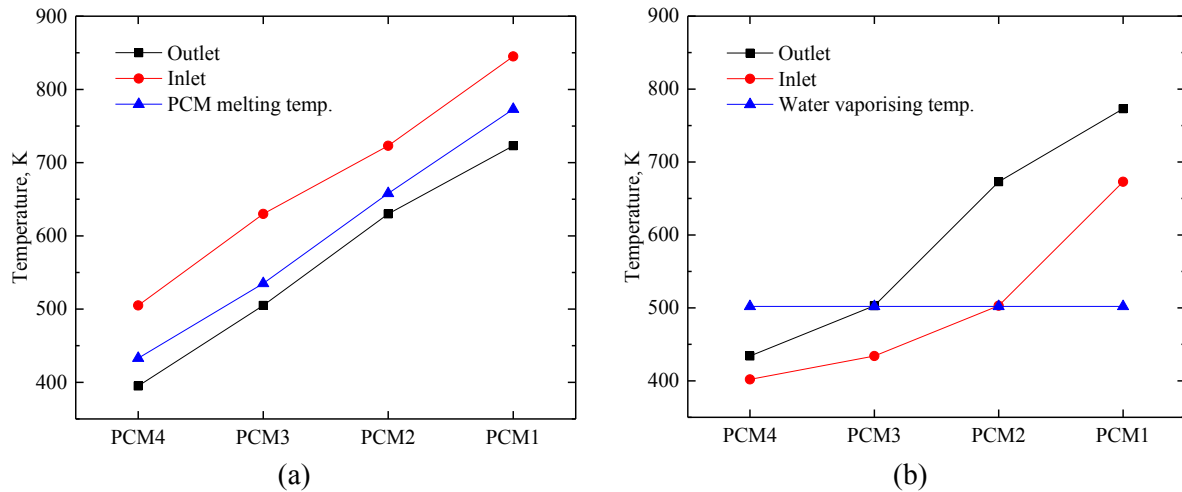
484
485

Figure 15: Real-time output power of the steam turbines during load-following operation.



486
487
488
489

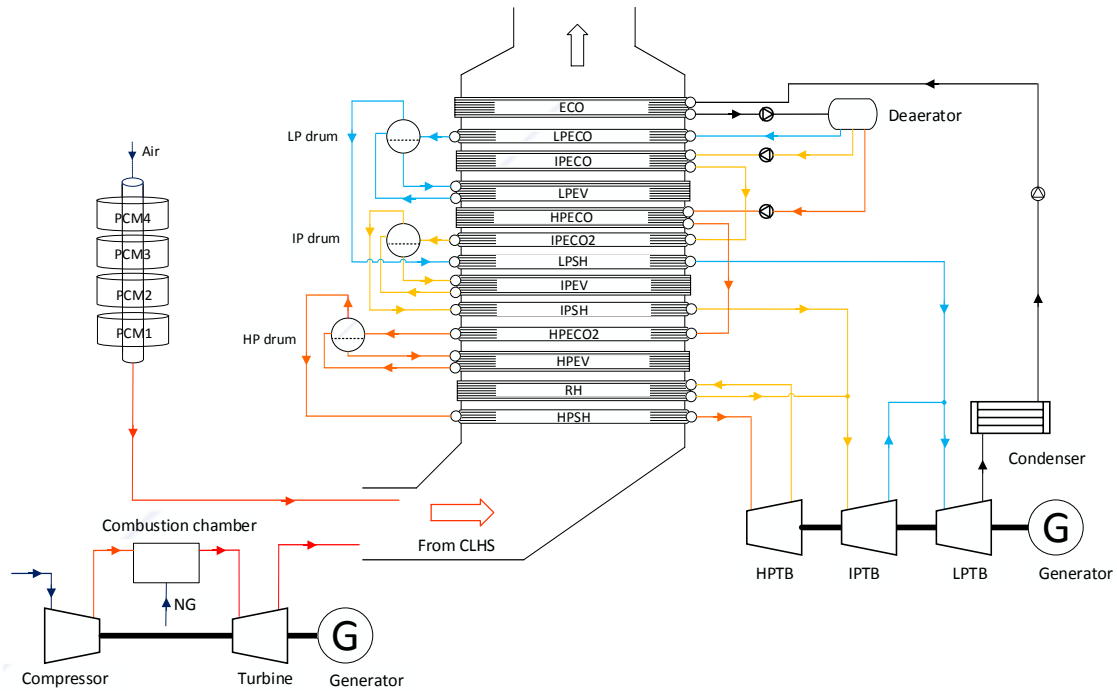
Figure 16: Amount of heat stored and released over charging and discharging during load-following operation.



490 Figure 17: Inlet and outlet temperature at each PCM layer at the end of charging (a) and discharging
 491 (b) during load-following operation.
 492

493 4.3 CLHS integration strategy during plant standstill

494 According to the initial temperature of the material, the start-up procedure of the CCGT power plant
 495 can be divided into: hot, warm and cold start depending on the initial temperature of the material, with
 496 standstill for up to 8 hours, 48 hours and 120 hours, respectively [1]. The start-up speed is limited by
 497 the thermal stress of the steam turbine and HRSG. The longer the standstill time, the longer the
 498 start-up time is required if there is no heat preservation measure adopted. Therefore, keeping the
 499 HRSG warm is crucial vital for the CCGT power plant to restart faster. In fact, the stored thermal
 500 energy can also be used to keep HRSG warm during plant standstill period. As shown in Figure 18,
 501 during the off-load period, ambient air is fed into the CLHS to produce hot air, which is then sent to
 502 the HRSG to compensate for the heat loss of the HRSG, thereby keeping the HRSG in a hot or warm
 503 state ready for faster start-up. The potential approach is to keep the HRSG warm through the CLHS
 504 instead of maintaining the natural circulation, so the gas turbine and steam turbines can be shut down.
 505 This approach does not change the inherent structure of the HRSG and the working fluid, there should
 506 be no major technical barrier in the implementation process. In addition, the air flow rate fed into the
 507 CLHS is determined by the current temperature drop in the CLHS, and this process can be controlled
 508 by a feedback loop.



509

510

Figure 18: CLHS integration strategy for discharging during plant standstill.

511

512 5. Conclusions

513 This paper describes the dynamic modelling and simulation study for CLHS integration into a 420
 514 MW CCGT power plant for flexible plant operation. A modelling method is introduced to achieve
 515 whole system dynamic simulation in Aspen Plus by an external FORTRAN code. The integration
 516 strategies during start-up, load-following and standstill operations are proposed and studied.

517

518 The dynamic simulation results shown that the strategies for CLHS integration with CCGT power
 519 plant is technically feasible. In the plant start-up processes, the gas turbine exhaust gas could pass
 520 through CLHS before discharged into atmosphere, and then the waste heat can be captured by CLHS.
 521 During the load-following operation, the output power of the CCGT power plant can be reduced by
 522 extracting exhaust gas from the gas turbine, the extracted exhaust gas is used to charge the CLHS; and
 523 the stored heat can be discharged to produce high temperature and high pressure steam for the steam
 524 turbine to increase the output power. Meanwhile the gas turbine section is still running at the rated
 525 load condition. Besides, the stored heat can also be used to maintain the HRSG under warm condition
 526 to reduce restart-up time after a standstill.

527

528 To further improve the CLHS performance under various operating models, efforts could be directed
 529 to its optimising design, such as optimising the layout of phase change materials according their
 530 thermodynamic properties, and the air flow rate used to keep the HRSG warm during a standstill.

531

532 Acknowledgements

533 The authors would like to acknowledge the support of the Engineering and Physical Research Council
 534 (EPSRC) for their support for the project - Flexible and Efficient Power Plant: Flex-E-Plant (Grant
 535 number: EP/K021095/1 and EP/M01536X/1) and also the grant support from EPSRC (EP/ L019469).

536 We also thank the following partners for their the valuable contributions: GE Energy, Doosan
 537 Babcock Limited, Centrica plc., EDF Energy (West Burton Power) Limited., Uniper Technologies
 538 Limited, Goodwin Steel Castings Limited, NPL Management Limited, R-MC Power Recovery
 539 Limited., RWE Generation UK plc., Scottish and Southern Energy (SSE) plc., Siemens Industrial
 540 Turbomachinery, and TWI Limited. The authors wish to thank the China Scholarship Council (CSC)
 541 for the PhD scholarship. The authors would like to thank the support from China Nation Basic
 542 Research Program 973 (2015CB251301).

543

544 **Nomenclature**

<u>Abbreviations</u>		
CCGT	combined-cycle gas turbine	
CHP	combined heat and power	
ECO	economizer	
HPECO	high pressure economizer	
HPEV	high pressure evaporator	
HPSH	high pressure superheater	
HPTB	high pressure turbine	
HRSG	heat recovery steam generator	
IPECO	intermediate pressure economizer	
IPEV	intermediate pressure evaporator	
IPSH	intermediate pressure superheater	
IPTB	intermediate pressure turbine	
LPECO	low pressure economizer	
LPEV	low pressure evaporator	
LPSH	low pressure superheater	
LPTB	low pressure turbine	
NG	natural gas	
PCM	phase change material	
RH	reheater	
TES	thermal energy storage	
<u>Symbols</u>		
A	Heat exchange area	m^2
c_p	Heat capacity	$J / (kg \cdot K)$
f	Weighting factor	
h	Enthalpy	J / kg
k	Heat conduction coefficient	$W / (m \cdot K)$
L	Enthalpy of phase change	$kJ \cdot kg^{-1}$
m	Mass flow rate	kg / s
\dot{m}_i	Ratio of mass flow rate to its designed value	
\dot{n}_i	Ratio of rotation speed to its designed value	
P	Pressure	Pa
Q	Heat flux of working fluid	W

r	Radius	m
t	Time	s
T	Temperature	K
T_c	Cold side temperature	K
T_h	Hot side temperature	K
ΔT	Temperature difference between hot side and cold side	K
U	Heat transfer coefficient	$W / m^2 K$
v	Working fluid velocity	m / s
V	Volume	m^3
W	Work done on the fluid	W
W_{in}	Power input	W
$W_{in,ideal}$	Power input under ideal polytropic condition	W
W_{out}	Power output	W
$W_{out,ideal}$	Power output under ideal isentropic condition	W
z	Length	m
η_c	Compressor polytropic efficiency	
η_t	Turbine isentropic efficiency	
θ	Angle	rad
γ	Specific heat ratio	
ρ	Density	kg / m^3
<u>Subscript</u>		
i	Cell number	
in	Inlet stream to a process unit	
out	Outlet stream from a process unit	

545

546

547 **References**

548 [1] N. Mertens, F. Alobaid, T. Lanz, B. Epple, and H.-G. Kim, "Dynamic simulation of a
549 triple-pressure combined-cycle plant: Hot start-up and shutdown," *Fuel*, vol. 167, pp. 135-148,
550 2016.

551 [2] A. Tică, H. Guéguen, D. Dumur, D. Faille, and F. Davelaar, "Design of a combined cycle
552 power plant model for optimization," *Applied energy*, vol. 98, pp. 256-265, 2012.

553 [3] F. Alobaid, R. Postler, J. Ströhle, B. Epple, and H.-G. Kim, "Modeling and investigation
554 start-up procedures of a combined cycle power plant," *Applied Energy*, vol. 85, pp.
555 1173-1189, 2008.

- 556 [4] A. Benato, S. Bracco, A. Stoppato, and A. Mirandola, "Dynamic simulation of combined
557 cycle power plant cycling in the electricity market," *Energy Conversion and Management*, vol.
558 107, pp. 76-85, 2016.
- 559 [5] S. Afanasyeva, C. Breyer, and M. Engelhard, "The Impact of Cost Dynamics of Lithium-Ion
560 Batteries on the Economics of Hybrid PV-Battery-GT Plants and the Consequences for
561 Competitiveness of Coal and Natural Gas-Fired Power Plants," in *Proceedings of the 10th
562 International Renewable Energy Storage Conference*, 2016.
- 563 [6] K. M. Powell and T. F. Edgar, "Modeling and control of a solar thermal power plant with
564 thermal energy storage," *Chemical Engineering Science*, vol. 71, pp. 138-145, 2012.
- 565 [7] S. Kuravi, J. Trahan, D. Y. Goswami, M. M. Rahman, and E. K. Stefanakos, "Thermal energy
566 storage technologies and systems for concentrating solar power plants," *Progress in Energy
567 and Combustion Science*, vol. 39, pp. 285-319, 2013.
- 568 [8] S. M. Flueckiger, B. D. Iverson, S. V. Garimella, and J. E. Pacheco, "System-level simulation
569 of a solar power tower plant with thermocline thermal energy storage," *Applied Energy*, vol.
570 113, pp. 86-96, 2014.
- 571 [9] T. Nuytten, B. Claessens, K. Paredis, J. Van Bael, and D. Six, "Flexibility of a combined heat
572 and power system with thermal energy storage for district heating," *Applied energy*, vol. 104,
573 pp. 583-591, 2013.
- 574 [10] J. D. Wojcik and J. Wang, "Technical feasibility study of thermal energy storage integration
575 into the conventional power plant cycle," *Energies*, vol. 10, p. 205, 2017.
- 576 [11] D. Li and J. Wang, "Study of supercritical power plant integration with high temperature
577 thermal energy storage for flexible operation," *Journal of Energy Storage*, vol. 20, pp.
578 140-152, 2018.
- 579 [12] N. Ceccarelli, M. van Leeuwen, T. Wolf, P. van Leeuwen, R. van der Vaart, W. Maas, *et al.*,
580 "Flexibility of low-CO₂ gas power plants: Integration of the CO₂ capture unit with CCGT
581 operation," *Energy Procedia*, vol. 63, pp. 1703-1726, 2014.
- 582 [13] Y. Hu, X. Li, H. Li, and J. Yan, "Peak and off-peak operations of the air separation unit in
583 oxy-coal combustion power generation systems," *Applied energy*, vol. 112, pp. 747-754,
584 2013.
- 585 [14] Y. Hu, A. Tewari, L. Varga, H. Li, and J. Yan, "System dynamics of oxyfuel power plants
586 with liquid oxygen energy storage," *Energy Procedia*, vol. 142, pp. 3727-3733, 2017.
- 587 [15] M. Hübel, S. Meinke, M. T. Andrén, C. Wedding, J. Nocke, C. Gierow, *et al.*, "Modelling and
588 simulation of a coal-fired power plant for start-up optimisation," *Applied Energy*, vol. 208, pp.
589 319-331, 2017.
- 590 [16] Y. Zhao, C. Wang, M. Liu, D. Chong, and J. Yan, "Improving operational flexibility by
591 regulating extraction steam of high-pressure heaters on a 660 MW supercritical coal-fired
592 power plant: A dynamic simulation," *Applied Energy*, vol. 212, pp. 1295-1309, 2018.
- 593 [17] A. Sciacovelli, Y. Li, H. Chen, Y. Wu, J. Wang, S. Garvey, *et al.*, "Dynamic simulation of
594 Adiabatic Compressed Air Energy Storage (A-CAES) plant with integrated thermal
595 storage—Link between components performance and plant performance," *Applied energy*, vol.
596 185, pp. 16-28, 2017.
- 597 [18] E. Pihl, S. Heyne, H. Thunman, and F. Johnsson, "Highly efficient electricity generation from
598 biomass by integration and hybridization with combined cycle gas turbine (CCGT) plants for
599 natural gas," *Energy*, vol. 35, pp. 4042-4052, 2010.

- 600 [19] R. Canepa and M. Wang, "Techno-economic analysis of a CO₂ capture plant integrated with
601 a commercial scale combined cycle gas turbine (CCGT) power plant," *Applied Thermal*
602 *Engineering*, vol. 74, pp. 10-19, 2015.
- 603 [20] A. Mathisen, H. Sørensen, M. C. Melaaen, and G.-I. Müller, "Investigation into optimal CO₂
604 concentration for CO₂ capture from aluminium production," 2013.
- 605 [21] J. François, L. Abdelouahed, G. Mauviel, M. Feidt, C. Rogeau, O. Mirgoux, *et al.*,
606 "Estimation of the energy efficiency of a wood gasification CHP plant using Aspen Plus,"
607 *Chem. Eng. Trans*, vol. 29, pp. 769-774, 2012.
- 608 [22] T. Adams and N. Mac Dowell, "Off-design point modelling of a 420MW CCGT power plant
609 integrated with an amine-based post-combustion CO₂ capture and compression process,"
610 *Applied Energy*, vol. 178, pp. 681-702, 2016.
- 611 [23] P. M. Mathias, H. C. Klotz, and J. M. Prausnitz, "Equation-of-state mixing rules for
612 multicomponent mixtures: the problem of invariance," *Fluid Phase Equilibria*, vol. 67, pp.
613 31-44, 1991.
- 614 [24] W. Wagner and A. Pruß, "The IAPWS formulation 1995 for the thermodynamic properties of
615 ordinary water substance for general and scientific use," *Journal of physical and chemical*
616 *reference data*, vol. 31, pp. 387-535, 2002.
- 617 [25] S. M. H. Mahmood, M. G. Turner, and K. Siddappaji, "Flow characteristics of an optimized
618 axial compressor rotor using smooth design parameters," in *ASME Turbo Expo 2016:*
619 *Turbomachinery Technical Conference and Exposition*, 2016, pp.
620 V02CT45A018-V02CT45A018.
- 621 [26] M. Ameri, P. Ahmadi, and S. Khanmohammadi, "Exergy analysis of a 420 MW combined
622 cycle power plant," *International Journal of Energy Research*, vol. 32, pp. 175-183, 2008.
- 623 [27] M. T. Mansouri, P. Ahmadi, A. G. Kaviri, and M. N. M. Jaafar, "Exergetic and economic
624 evaluation of the effect of HRSG configurations on the performance of combined cycle power
625 plants," *Energy Conversion and Management*, vol. 58, pp. 47-58, 2012.
- 626 [28] N. Zhang and R. Cai, "Analytical solutions and typical characteristics of part-load
627 performances of single shaft gas turbine and its cogeneration," *Energy Conversion and*
628 *Management*, vol. 43, pp. 1323-1337, 2002.
- 629 [29] S. Quoilin, R. Aumann, A. Grill, A. Schuster, V. Lemort, and H. Spliethoff, "Dynamic
630 modeling and optimal control strategy of waste heat recovery Organic Rankine Cycles,"
631 *Applied Energy*, vol. 88, pp. 2183-2190, 2011.
- 632 [30] B. Tashtoush, M. Molhim, and M. Al-Rousan, "Dynamic model of an HVAC system for
633 control analysis," *Energy*, vol. 30, pp. 1729-1745, 2005.
- 634 [31] D. Li, Y. Hu, W. He, and J. Wang, "Dynamic modelling and simulation of a combined-cycle
635 power plant integration with thermal energy storage," in *Automation and Computing (ICAC),*
636 *2017 23rd International Conference on*, 2017, pp. 1-6.
- 637 [32] F. Agyenim, N. Hewitt, P. Eames, and M. Smyth, "A review of materials, heat transfer and
638 phase change problem formulation for latent heat thermal energy storage systems
639 (LHTESS)," *Renewable and sustainable energy reviews*, vol. 14, pp. 615-628, 2010.
- 640 [33] W. Zhao, D. M. France, W. Yu, T. Kim, and D. Singh, "Phase change material with graphite
641 foam for applications in high-temperature latent heat storage systems of concentrated solar
642 power plants," *Renewable Energy*, vol. 69, pp. 134-146, 2014.

- 643 [34] K. Lafdi, O. Mesalhy, and A. Elgafy, "Graphite foams infiltrated with phase change materials
644 as alternative materials for space and terrestrial thermal energy storage applications," *Carbon*,
645 vol. 46, pp. 159-168, 2008.
- 646 [35] B. Cárdenas and N. León, "High temperature latent heat thermal energy storage: Phase
647 change materials, design considerations and performance enhancement techniques,"
648 *Renewable and sustainable energy reviews*, vol. 27, pp. 724-737, 2013.
- 649 [36] M. M. Kenisarin, "High-temperature phase change materials for thermal energy storage,"
650 *Renewable and Sustainable Energy Reviews*, vol. 14, pp. 955-970, 2010.
- 651 [37] S. Patankar, *Numerical Heat Transfer and Fluid Flow*: McGraw Hill, 1980.
- 652 [38] P. Verma and S. Singal, "Review of mathematical modeling on latent heat thermal energy
653 storage systems using phase-change material," *Renewable and Sustainable Energy Reviews*,
654 vol. 12, pp. 999-1031, 2008.
- 655 [39] A. Gil, M. Medrano, I. Martorell, A. Lázaro, P. Dolado, B. Zalba, *et al.*, "State of the art on
656 high temperature thermal energy storage for power generation. Part 1—Concepts, materials
657 and modellization," *Renewable and Sustainable Energy Reviews*, vol. 14, pp. 31-55, 2010.
- 658 [40] F. Alobaid, S. Pfeiffer, B. Eppler, C.-Y. Seon, and H.-G. Kim, "Fast start-up analyses for
659 Benson heat recovery steam generator," *Energy*, vol. 46, pp. 295-309, 2012.
- 660 [41] A. Pasha, "Combined cycle power plant start-up effects and constraints of the HRSG," in
661 *ASME 1992 International Gas Turbine and Aeroengine Congress and Exposition*, 1992, pp.
662 V004T11A016-V004T11A016.
- 663 [42] T. Kim, D. Lee, and S. Ro, "Analysis of thermal stress evolution in the steam drum during
664 start-up of a heat recovery steam generator," *Applied Thermal Engineering*, vol. 20, pp.
665 977-992, 2000.
- 666 [43] X. Luo, J. Wang, J. D. Wojcik, J. Wang, D. Li, M. Draganescu, *et al.*, "Review of Voltage
667 and Frequency Grid Code Specifications for Electrical Energy Storage Applications,"
668 *Energies*, vol. 11, pp. 1-26, 2018.

669